The Astrophysical Journal, 891:126 (13pp), 2020 March 10 https://doi.org/10.3847/1538-4357/ab7207

Inverse First Ionization Potential Effects in Giant Solar Flares Found from Earth X-Ray Albedo with *Suzaku*/XIS

Satoru Katsuda[1], Masanori Ohno[2,3,4,5], Koji Mori[6], Tatsuhiko Beppu[6], Yoshiaki Kanemaru[6], Makoto S. Tashiro[1,7], Yukikatsu Terada[1,7], Kosuke Sato[1], Kae Morita[1], Hikari Sagara[1], Futa Ogawa[1], Haruya Takahashi[1], Hiroshi Murakami[8], Masayoshi Nobukawa[9], Hiroshi Tsunemi[10], Kiyoshi Hayashida[7,10,11], Hironori Matsumoto[10,11], Hirofumi Noda[10,11], Hiroshi Nakajima[12], Yuichiro Ezoe[13], Yohko Tsuboi[14], Yoshitomo Maeda[7], Takaaki Yokoyama[15], and Noriyuki Narukage[16]
[1] Graduate School of Science and Engineering, Saitama University, 255 Shimo-Ohkubo, Sakura, Saitama 338-8570, Japan
[2] Institute of Physics, Eötvös University, Pázmány Péter sétány 1/A, Budapest, 1117, Hungary
[3] MTA-Eötvös University, Lendület Hot Universe and Astrophysics Research Group, Budapest, Hungary
[4] Konkoly Observatory of the Hungarian Academy of Sciences, Konkoly-Thege ut 15-17, Budapest, 1121, Hungary
[5] School of Science, Hiroshima University, 1-3-1, Kagamiyama, Higashi-Hiroshima, Hiroshima 739-8526, Japan
[6] Department of Applied Physics and Electronic Engineering, University of Miyazaki, 1-1, Gakuen Kibanadai-nishi, Miyazaki 889-2192, Japan
[7] Japan Aerospace Exploration Agency, Institute of Space and Astronautical Science, 3-1-1 Yoshino-dai, Chuo-ku, Sagamihara, Kanagawa 252-5210, Japan
[8] Faculty of Liberal Arts, Tohoku Gakuin University, 2-1-1 Tenjinzawa, Izumi-ku, Sendai, Miyagi 981-3193, Japan
[9] Department of Teacher Training and School Education, Nara University of Education, Takabatake-cho, Nara, Nara 630-8528, Japan
[10] Department of Earth and Space Science, Osaka University, 1-1 Machikaneyama-cho, Toyonaka, Osaka 560-0043, Japan
[11] Project Research Center for Fundamental Sciences, Osaka University, 1-1 Machikaneyama-cho, Toyonaka, Osaka 560-0043, Japan
[12] College of Science and Engineering, Kanto Gakuin University, 1-50-1 Mutsuurahigashi, Kanazawa-ku, Yokohama, Kanagawa 236-8501, Japan
[13] Department of Physics, Tokyo Metropolitan University, 1-1 Minami-Osawa, Hachioji, Tokyo 192-0397, Japan
[14] Department of Physics, Chuo University, 1-13-27 Kasuga, Bunkyo, Tokyo 112-8551, Japan
[15] Department of Earth and Planetary Science, The University of Tokyo, 7-3-1 Hongo, Bunkyo-ku, Tokyo 113-0033, Japan
[16] National Astronomical Observatory of Japan, National Institutes of Natural Science, 2-21-1 Osawa, Mitaka, Tokyo 181-8588, Japan
Received 2019 December 20; revised 2020 January 26; accepted 2020 January 28; published 2020 March 12

Abstract

We report X-ray spectroscopic results for four giant solar flares that occurred on 2005 September 7 (X17.0), 2005 September 8 (X5.4), 2005 September 9 (X6.2), and 2006 December 5 (X9.0), obtained from Earth albedo data with the X-ray Imaging Spectrometer (XIS) on board *Suzaku*. The good energy resolution of the XIS (FWHM $\sim$ 100 eV) enables us to separate a number of line-like features and detect the underlying continuum emission. These features include Si Heα, Si Lyα, S Heα, S Lyα, Ar Heα, and Ca Heα originating from solar flares as well as fluorescent Ar Kα and Ar Kβ from the Earth's atmosphere. Absolute elemental abundances (X/H) averaged over the four flares are obtained to be $\sim$2.0 (Ca), $\sim$0.7 (Si), $\sim$0.3 (S), and $\sim$0.9 (Ar) at around flare peaks. This abundance pattern is similar to those of active stars' coronae showing inverse first ionization potential (i-FIP) effects, i.e., elemental abundances decrease with decreasing FIP with a turnover at the low end of the FIP. The abundances are almost constant during the flares, with the exception of Si which increases by a factor of $\sim$2 in the decay phase. The evolution of the Si abundance is consistent with the finding that the i-FIP plasma originates from chromospheric evaporation and then mixes with the surrounding low-FIP biased materials. Flare-to-flare abundance varied by a factor of two, agreeing with past observations of solar flares. Finally, we emphasize that Earth albedo data acquired by X-ray astronomy satellites like *Suzaku* and the *X-Ray Imaging Spectroscopy Mission* can significantly contribute to studies of solar physics.

Unified Astronomy Thesaurus concepts: Solar abundances (1474); Solar flares (1496); Solar corona (1483); Solar x-ray emission (1536); Solar x-ray flares (1816)

1. Introduction

Plasma composition is one of the keys to understanding the physical processes associated with mechanisms to transport, heat, and accelerate plasma in the solar atmosphere. In the second half of the 20th century, it was revealed that the elemental composition of the solar corona is different from that of the underlying photosphere by using extreme-ultraviolet and X-ray spectroscopy of the solar corona as well as in situ measurements of solar-energetic particles and solar winds. The discrepancy is understood to be caused by a dependence on the first ionization potential (FIP) of elements (e.g., Meyer 1985; Schmelz et al. 2012; Reames 2018). In the corona, elements with a low FIP ($\lesssim$10 eV) are enhanced by a factor of two to four compared with the photospheric abundances (e.g., Feldman 1992; Dennis et al. 2015).[17] This is widely known as the "FIP effect," but its mechanism has been one of the most enduring mysteries of solar physics, besides the well-known coronal heating problem.

It has been shown that coronae of inactive stars exhibit similar solar-like FIP effects (Drake et al. 1997; Laming & Drake 1999). In contrast, later spectral types with stronger magnetic fields show an "inverse FIP (i-FIP) effect," i.e., low-FIP elements are underabundant relative to high-FIP elements (e.g., Brinkman et al. 2001; Güdel et al. 2001; Audard et al. 2003; Huenemoerder et al. 2003; Sanz-Forcada et al. 2003; Argiroffi et al. 2004). There is a clear relation between the FIP bias (defined by the ratio of elemental abundance in the corona to that in the photosphere) and the spectral type; early G stars all have a solar-like FIP effect, which decreases toward early K stars, reaching no FIP effect at about K5, and then reverses to the i-FIP effect for later than K stars with the magnitude of the effect increasing with spectral type (Wood & Linsky 2010; Wood et al. 2018). For active stars showing i-FIP effects, the

[17] However, it has been still debated whether low-FIP elements are enhanced or high-FIP elements are depleted relative to the photospheric values (e.g., Veck & Parkinson 1981; Raymond et al. 1997).

abundances decrease with decreasing FIP. However, there is emerging evidence that a turnover occurs at a very low FIP, below which the elemental abundances steeply increase (e.g., Huenemoerder et al. 2013). The origin of the turnover remains unclear. Substantial effort has been devoted to interpreting the FIP fractionation, and there is a consensus that the fractionation results from a separation of ions and neutrals in the upper chromosphere with a temperature of 6000–10,000 K, where low-FIP elements are ionized but high-FIP elements are mostly in neutral states. Among several theoretical models proposed (e.g., Henoux 1998), the only model that can explain both FIP and i-FIP effects is the Laming model, which is involved in ponderomotive forces, a nonlinear force that a charged particle experiences in an inhomogeneous oscillating electromagnetic field (Laming 2004, 2009, 2012, 2015). Ponderomotive forces in the chromosphere may, in principle, be directed upward or downward, resulting in FIP and i-FIP effects, respectively. Since upward ponderomotive forces are common in a solar condition, i.e., the Alfvén wave energy flux through the chromosphere is nonzero (see Section 3.2 in Laming 2004, for more details), we generally see enhancements of low-FIP elements in the solar corona. In coronal holes with open-field lines, upward ponderomotive forces are expected to become very weak, and thus a very low FIP effect is expected there, which is indeed observed (Feldman & Widing 1993). In sunspots, where p-mode waves probably convert to fastmode waves and the fastmode waves get reflected back toward the chromosphere (Laming 2015), downward ponderomotive forces are expected. Therefore, it is reasonable that i-FIP effects are observed in magnetically active stars whose surfaces are largely covered by starspots.

Elemental abundances during solar flares have been reported to be coronal or intermediate between the coronal and photospheric values (Sterling et al. 1993; Sylwester et al. 1998, 2015; Fludra & Schmelz 1999; Phillips & Dennis 2012; Narendranath et al. 2014; Dennis et al. 2015). However, it was recently realized that the abundance pattern is different from coronal abundances, in that the boundary between low-FIP and high-FIP elements is about 7 eV (Dennis et al. 2015), significantly less than ∼10 eV that is normally observed for solar coronae or solar-energetic particles. This implies that the fractionation of flare plasmas are cool and expected to be in lower chromospheric altitudes than that of the normal coronal plasma. In fact, a few observations of solar flares showed nearly photospheric abundances (Veck & Parkinson 1981; Warren 2014), indicating that the bulk of the plasma evaporated during a flare comes from deep in the chromosphere (Warren 2014).

Recently, Doschek et al. (2015) discovered the i-FIP effect on the Sun, for the first time. They found unexpectedly high Ar XIV/Ca XIV intensity ratios in small regions near sunspots during solar flares. Since Ar and Ca are high- and low-FIP elements, respectively, the result agrees with the prediction of the Laming model. One important question is whether the i-FIP effect is caused by an enhancement of the high-FIP element or a depletion of the low-FIP element. In the Laming model, we expect the latter case, because the ponderomotive force is effective only to low-FIP elements. Doschek & Warren (2016) estimated the path length of the plasma to be smaller than what is expected for the plasma with photospheric abundances, suggesting the depletion of the low-FIP elements. More recently, Brooks (2018) pointed out that coronal loops showing i-FIP effects persisted for ∼40 minutes, which is over a factor of four longer than the lifetime of the other loops exhibiting normal FIP effects. This indicates the depletion of the low-FIP elements in the i-FIP regions.

Suzaku was the fifth in a series of Japanese X-ray astronomy satellites, launched on 2005 July 10 (Mitsuda et al. 2007). It was devoted to observations of celestial X-ray sources, whereas a large amount of Earth albedo of the solar X-ray emission was observed as a by-product, because of its low-Earth orbit at 550 km altitude combined with the 3D fixed attitude during each observation. The Earth albedo data were obtained almost every orbit or ∼96 minutes, when the telescope pointed at the bright Earth illuminated by the Sun (the duration is typically several minutes every orbit). Therefore, *Suzaku* monitored the Sun throughout the 10 yr lifetime of its mission with a ∼96 minutes cadence.

Suzaku carried three distinct coaligned scientific instruments. The primary instrument was an X-ray microcalorimeter, which unfortunately became inoperable before performing observations due to unexpected evaporation of liquid helium coolant in the early commissioning phase. The remaining two instruments, X-ray sensitive imaging CCD cameras (the X-ray Imaging Spectrometer, XIS; Koyama et al. 2007) and a nonimaging collimated Hard X-ray Detector (Takahashi et al. 2007) worked well through the entire mission. In this paper, we focus on the thermal X-ray emission from the Sun, concentrating on the data taken by the XIS which covers an energy range of 0.2–12 keV.

We present absolute elemental abundances of Si, S, Ar, and Ca (relative to H) for four flares with *GOES* classes from X5.4 to X17.0, based on line-to-continuum ratios. Absolute abundances are much more difficult to determine than relative abundances, because most of the hydrogen in the corona is ionized and no observable spectral lines are produced. The amount of hydrogen (and helium) must be obtained by continuum emission. This is generally difficult with solar high-resolution dispersive spectrometers for several possible reasons, such as instrumental fluorescence background emission, an improper shape for instrumental spectral response (Sylwester et al. 2002). Some nondispersive spectrometers had the capability to reliably measure continuum emission, but their spectral resolutions were poor, e.g., FWHM ∼ 600 eV at 5.9 keV for MESSENGER/SAX (Dennis et al. 2015), FWHM ∼ 200 eV at 5.9 keV for *Chandrayaan-1*/XSM (Narendranath et al. 2014), and FWHM ∼ 150 eV in 0.2–4 keV for Amptek/X123-SDD (Caspi et al. 2015), hampering reliable measurements of absolute abundances. In this way, significant systematic uncertainties still remain on coronal absolute abundances. Thanks to the stable and low background of the XIS (Tawa et al. 2008) combined with better spectral resolution of $E/\Delta E \sim 20$ or FWHM ∼ 120 eV at 3 keV than other nondispersive spectrometers, we measured the cleanest line-to-continuum ratios and absolute elemental abundances. We present the data and their reduction in Section 2, and perform spectral analyses in Section 3. The results are discussed in Section 4. More details on the data reduction and the simulation to examine spectral deformation due to Earth albedo are given in Appendices A and B, respectively. The errors quoted in this paper are at the 1σ confidence level, unless otherwise stated.

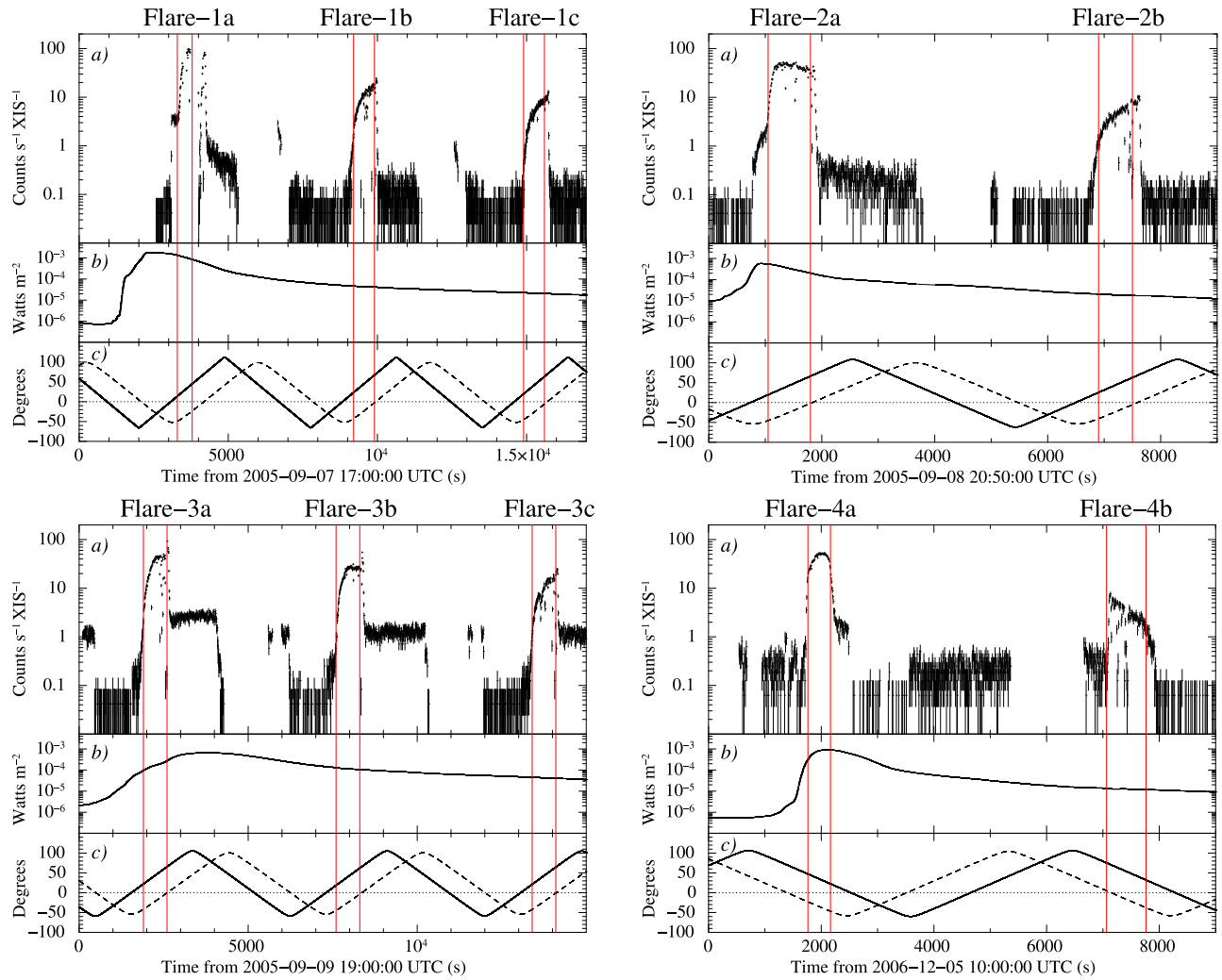

Figure 1. Light curves of the four flares. The upper panels, labeled a), show XIS data averaged for the two or three front-illuminated CCDs in the 1.65–5 keV band. Middle panels, labeled b), show *GOES* X-ray fluxes in 1–8 Å. The bottom panels, labeled c), show *Suzaku*'s (dashed lines) and the Sun's (solid lines) elevation angles measured from the Earth limb. The red vertical lines indicate the time periods when we extracted the XIS spectra.

2. Observations and Data Reduction

Earth albedo emission observed with *Suzaku*/XIS is spatially unresolved full disk integrated emission of the Sun, and thus consists of various components such as active regions, quiet regions, and flares. However, at a large, say *GOES* X-class, solar flare event, flare emission itself dominates the observed X-ray emission by ∼90%–99%, as can be seen from the light curves and spectra in Figures 1 and 4. In such cases, we obtain nearly pure flare emission. In addition, the large X-ray fluxes allow us to obtain enough photons for detailed spectroscopy. Therefore, we focus on only large flares in this paper.

Fifty nine X-class flares occurred during the period when *Suzaku* was in operation. Among them, 14 flares were captured when *Suzaku* pointed at the bright Earth. Although these 14 flares allowed us to obtain sufficient photons for our spectral analysis, we further selected early-epoch four flares, i.e., Flares-1, 2, 3, and 4 occurred on 2005 September 7 (X17.0), 2005 September 8 (X5.4), 2005 September 9 (X6.2), and 2006 December 5 (X9.0), respectively. This is because these early-epoch data have the best spectral resolution; spectral resolution of the XIS degrades with time due to the integrated radiation damage of CCDs. Quantitatively, we set a criterion that one-sigma width of fluorescent Ar Kα is less than 50 eV. With this energy resolution, we can clearly separate fluorescent Ar Kα and Ar Kβ lines, which is necessary to measure the line intensity of the Ar Heα complex located between the two fluorescences. Throughout this paper, we use only front-illuminated CCDs, i.e., XIS0, 2, 3, because they have slightly better spectral resolution than the back-illuminated CCD, XIS1.

Information about *Suzaku* observations used in this paper is summarized in Table 1. As described in Section 1, the spacecraft attitude is 3D fixed, and thus the scattering angle of solar X-rays at the Earth's atmosphere is fixed during one observational sequence. The scattering angle can be calculated by "180 − (XRT-Sun angle) degrees," where the XRT-Sun angle is the angle between the telescope axis and direction to the Sun. The scattering angles were close to each other, agreeing within 7° for the three observations of our interest.

We reprocessed the XIS data, following the standard screening criteria[18] recommended by the calibration team of *Suzaku*. One exception is the elevation angle, for which we changed the selection criteria from "ELV > 5 & DYE_ELV > 20" (by default) to "ELV < −10 & NTE_ELV > 5" in order to extract the bright Earth data. In addition, we developed a new method

[18] Section 6.3 in http://heasarc.gsfc.nasa.gov/docs/suzaku/analysis/abc.

Table 1
Suzaku Observations Used in this Paper

Observation ID	Flare ID	Start Time[a]	XRT-Sun Angle (deg)	Scattering Angle (deg)	Effective Exposure Time (s)[b]
100019010	Flare-1a	2005 Sep 7 17:54:50	75.1	104.9	315 (×3 CCDs)
100019010	Flare-1b	2005 Sep 7 19:33:20	75.1	104.9	700 (×3 CCDs)
100019010	Flare-1c	2005 Sep 7 21:08:20	75.1	104.9	700 (×3 CCDs)
100019010	Flare-2a	2005 Sep 8 21:07:30	75.1	104.9	750 (×3 CCDs)
100019010	Flare-2b	2005 Sep 8 22:45:00	75.1	104.9	700 (×3 CCDs)
100019020	Flare-3a	2005 Sep 9 19:31:40	70.9	109.1	700 (×3 CCDs)
100019020	Flare-3b	2005 Sep 9 21:06:40	70.9	109.1	700 (×3 CCDs)
100019020	Flare-3c	2005 Sep 9 22:43:20	70.9	109.1	700 (×3 CCDs)
801064010	Flare-4a	2006 Dec 5 10:29:24	68.1	111.9	400 (×2 CCDs)
801064010	Flare-4b	2006 Dec 5 11:57:44	68.1	111.9	700 (×2 CCDs)

Notes.
[a] Starting time when we extract the spectrum.
[b] The entire imaging area of XIS2 was lost in 2005 November possibly due to micrometeorite hits, so that only two XIS sensors were in operation during Flare-4.

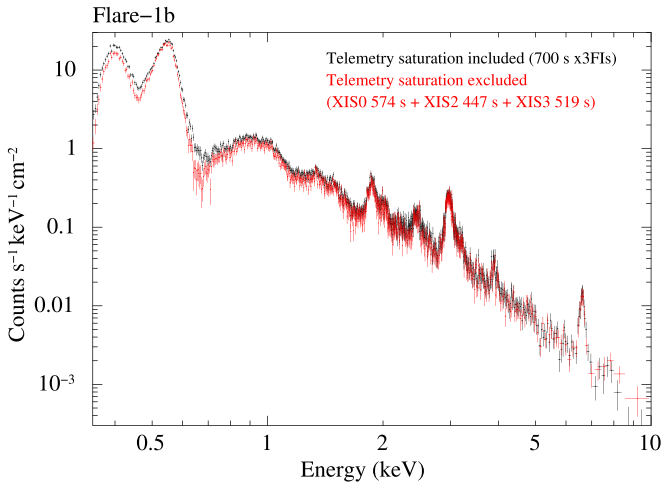

Figure 2. XIS spectra (three front-illuminated CCDs (FIs) combined) during Flare-1b. Black and red correspond to the one before and after excluding the time period of the telemetry saturation. The spectral quality of both is essentially the same as each other, except that the effective exposure time decreased by ∼30% after excluding the telemetry-saturation period.

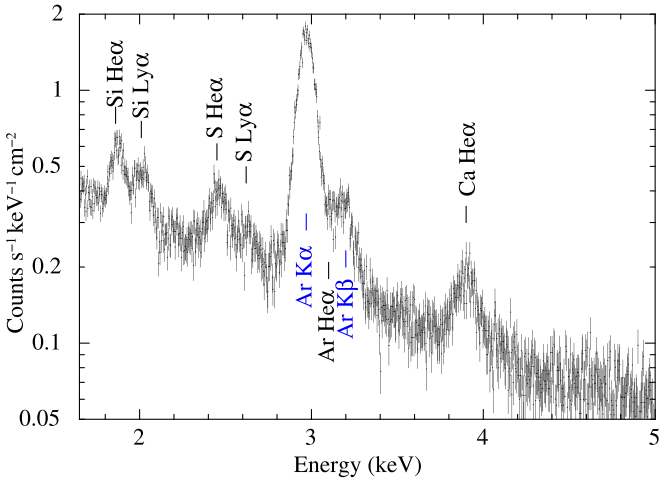

Figure 3. XIS spectrum (three FIs combined) during Flare-2a. This spectrum is before preflare subtraction. Prominent line features are identified.

to infer better backgrounds of the XIS. We describe detailed techniques of this method in Appendix A. Briefly, the method reestimates the dark level more precisely than the standard process does, based on information about 16 pixels surrounding each event island. This method is also effective to recover spectral resolution, especially for the data taken during time periods showing more rapid time variation of background than the onboard dark estimation, such as in the bright Earth observation.

In Figure 1, the top panels for each flare section show XIS light curves in the 1.65–5 keV band. They are averaged all over available (two or three) front-illuminated CCDs. The middle panels show *GOES* X-ray light curves, and the bottom panels show elevation angles of the telescope (dashed lines) and the Sun (solid lines) measured from the Earth's limb. In the XIS light curves, the high-count-rate periods represent the bright Earth observation, which are confirmed by the elevation angles of *Suzaku* and the Sun. The long-term variations of XIS light curves in the bright Earth periods follow *GOES* X-ray light curves. However, there are significant discrepancies between the XIS and *GOES* light curves within individual bright Earth periods. This is because the XIS count rate in the bright Earth period is affected not only by the intrinsic solar X-ray flux, but also by the elevation angles of both *Suzaku's* telescope and the Sun. Also, there are abruptly dropping XIS data points in the bright Earth periods. These are caused by the telemetry saturation. To check the effect of the telemetry saturation, we compare spectra before and after excluding the telemetry-saturation periods for Flare-1b, as shown in Figure 2. This comparison demonstrates that the telemetry saturation does not significantly affect the spectral shape, especially in the energy range of our interest, i.e., 1.65–5 keV. Thus, we decided to use telemetry-saturated data in our analysis; otherwise we lost all the exposure times for Flare-1a and Flare-2a.

Our target, bright Earth during giant solar flares, is indeed so bright that one may concern the pileup effects, i.e., more than one photon strikes the same CCD pixel, which generally results in a flux decrease and spectral hardening. Maeda et al. (2009) investigated the XIS data for the Cassiopeia A supernova remnant, one of the brightest diffuse X-ray sources, and concluded that pileup does not affect the XIS data. The XIS count rate of Cassiopeia A was about 118 s^{-1} for each front-illuminated CCD. This is comparable to that of Flare-1a, which shows the maximum count rate in the bright Earth. The emitting area of Cassiopeia A has about a radius of 3′, which is only ∼10% of the bright Earth data extending over the entire

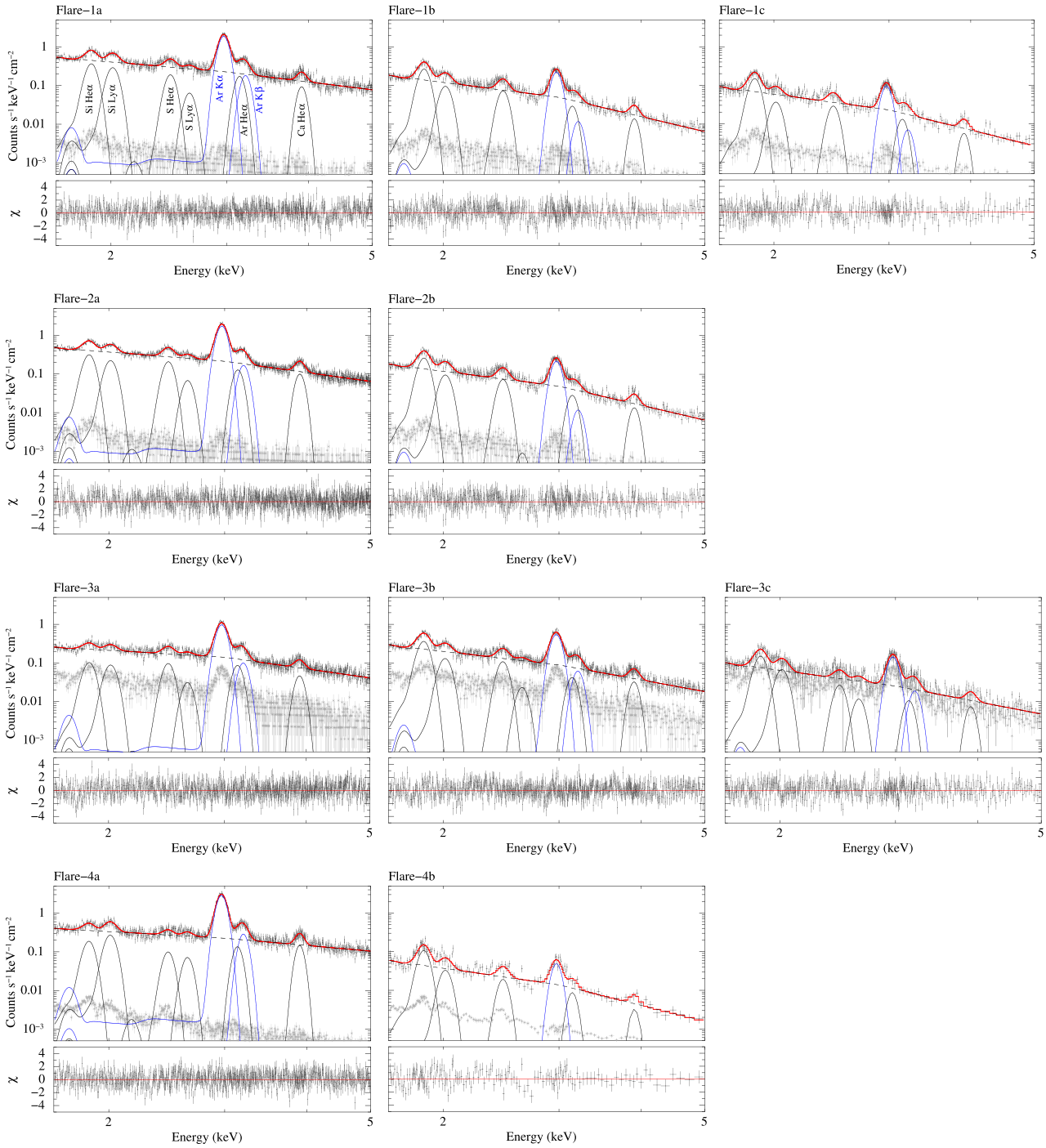

Figure 4. XIS spectra for Flare-1 to 4 from the top to bottom. The top panels in each case show the data together with the best-fit model consisting of eight Gaussians plus a broken power law. The total emission models are shown in red, whereas the thermal lines, continuum, and fluorescent lines are shown in solid black, dashed black, and blue lines, respectively. The gray data are the preflare backgrounds. The bottom panels in each case represent the residuals.

field of view of the XIS. Therefore, the surface brightness of the bright Earth is an order of magnitude smaller than that of Cassiopeia A, leading us to conclude that bright Earth is free from pileup effects.

As shown in Figure 1, the four flares of interest lasted much longer than *Suzaku*'s orbital period of 96 minutes. Therefore, we extracted XIS spectra from a few bright Earth periods for each flare (e.g., Flare-1a, Flare-1b, and Flare-1c). The effective exposure time for each spectrum is given in Table 1.

3. Spectral Analysis and Results

For a demonstration, we present *Suzaku*/XIS's bright Earth spectrum during Flare-2a in Figure 3. The data are the sum of the three XIS sensors before subtracting the preflare background which is only a 1% level of the source in the energy range of interest (see Figure 4). There are several prominent features above the underlying continuum emission. By fitting the spectrum with eight Gaussians plus a broken power-law component, we derived the line centroids, widths, and fluxes

Table 2
Line Properties Measured for Flare-2a

Line ID	Ion	Expected Energy (keV)[a]	Centroid (keV)	Broadening (keV)	Intensity (10^{-5} ph cm^{-2} s^{-1} arcmin^{-2})
Si Heα	Si^{12+}	1.839 (f), 1.854 + 1.855 (i), 1.865 (r)	1.869 ± 0.003	0.016 ± 0.007	$2.63^{+0.20}_{-0.18}$
Si Lyα	Si^{13+}	2.006	2.014 ± 0.005	0.014 ± 0.009	$1.48^{+0.15}_{-0.14}$
S Heα	S^{13+}	2.430 (f), 2.447 + 2.449 (i), 2.461 (r)	2.460 ± 0.006	0.028 ± 0.011	$1.672^{+0.21}_{-0.19}$
S Lyα	S^{14+}	2.623	$2.628^{+0.014}_{-0.017}$	0.019 (<0.048)	$0.54^{+0.19}_{-0.15}$
Ar Heα	Ar^{14+}	3.104 (f), 3.124 + 3.126 (i), 3.140 (r)	$3.135^{+0.034}_{-0.021}$	=Ca Heα	$1.28^{+0.86}_{-0.22}$
Ca Heα	Ca^{15+}	3.861 (f), 3.883 + 3.888 (i), 3.902 (r)	3.902 ± 0.006	0.035 ± 0.011	$1.03^{+0.10}_{-0.10}$
Ar Kα	Ar^{0+}	2.958	2.972 ± 0.001	0.021 ± 0.002	$14.70^{+0.28}_{-0.27}$
Ar Kβ	Ar^{0+}	3.191	=Ar Kα + 0.235	=Ar Kα	$1.55^{+0.27}_{-0.92}$

Note.
[a] (f), (i), and (r) represent forbidden, intercombination, and resonance lines, respectively.

Table 3
Equivalent Widths from Gaussians plus a Continuum Model[a]

Flare ID	Si Heα	Si Lyα	S Heα	Ar Heα	Ca Heα
Flare-1a	103 ± 5	72 ± 4	71 ± 5	109 ± 7	105 ± 8
Flare-1b	237 ± 7	80 ± 5	108 ± 7	92 ± 10	117 ± 15
Flare-1c	276 ± 13	62 ± 9	107 ± 14	125 ± 20	123 ± 31
Flare-2a	96 ± 3	62 ± 2	86 ± 3	87 ± 5	131 ± 5
Flare-2b	234 ± 7	83 ± 5	112 ± 7	92 ± 10	119 ± 15
Flare-3a	55 ± 5	44 ± 4	67 ± 5	94 ± 7	98 ± 7
Flare-3b	195 ± 6	69 ± 4	97 ± 6	75 ± 9	129 ± 11
Flare-3c	243 ± 12	112 ± 9	80 ± 14	67 ± 21	109 ± 25
Flare-4a	74 ± 6	81 ± 5	40 ± 5	80 ± 8	135 ± 8
Flare-4b	334 ± 20	90 ± 12	95 ± 18	97 ± 24	103 ± 37

Note.
[a] The values are in units of electronvolts.

summarized in Table 2. The line centroids allow us to identify them as Si Heα, Si Lyα, S Heα, S Lyα, and Ca Heα features together with fluorescent Ar Kα and Ar Kβ lines. The highly ionized features should originate from the Sun, whereas the fluorescent lines should arise from the Earth's atmosphere. If we expand the energy range of the XIS spectrum, we can identify some other features including fluorescent O Kα and N Kα around 0.5 keV as well as an Fe Heα complex and a possible Compton shoulder hump at ∼6.5 keV. In this paper, we will focus only on the intermediate-mass elements, i.e., Si, S, Ar, and Ca arising from the solar flares, because lines from these elements are cleaner than those from other elements such as Mg (contaminated by instrumental Al lines) and Fe (contaminated by emission reflected by the satellite). Analyses of other lines including fluorescent K lines from N, O, and Ar are ongoing, and will be presented elsewhere.

Figure 4 presents all the XIS spectra to be analyzed, i.e., the bright Earth data for the four flares. The data in black and gray are the sums of data and preflare backgrounds, respectively, for which we utilized only front-illuminated CCDs. The background spectra, shown in gray in Figure 4, are taken from preflare bright Earth for each flare. Since Flare-1 and Flare-2 occurred continuously, we used the same background taken prior to Flare-1. Redistribution matrix files (RMF) and auxiliary response files (ARF) were generated by using `xisrmfgen` and `xissimarfgen` (Ishisaki et al. 2007), respectively. Briefly, the RMF is a probability map from incident photon energy space into detector's calibrated pulse-height (PH) space, and the ARF gives effective areas as a function of a photon energy. These two files are convolved with a model spectrum to fit the data. Details of the RMF and ARF are described in Section 4 of Ishisaki et al. (2007).

3.1. Measuring Equivalent Widths

The spectral shape of solar X-ray emission is expected to be modified by the Earth's atmospheric scattering. This spectral deformation must be considered when interpreting the bright Earth data. In this work, we focus on equivalent widths (EWs), which are not affected by the spectral deformation, because both lines and their underlying continua are equally deformed. We measured EWs directly from the original data, and converted them to absolute elemental abundances.

We note that there is a pioneering work by Itoh et al. (2002) who analyzed the Earth albedo data obtained with *ASCA*. To take into account the albedo effects, they adopted the `hrefl` model in XSPEC (Arnaud 1996), which was developed by Dr Yaqoob to consider reflection by neutral matters. Itoh et al. (2002) assumed it to be a good approximation for the Earth albedo. This assumption may be good enough. However, it is technically difficult for the `hrefl` model to take into account the Earth's atmospheric abundances. Therefore, we did not use the `hrefl` model in our analyses, but relied on EWs that are free from spectral deformation.

We fitted the data with a simple combination model consisting of eight Gaussians and a continuum model. The eight Gaussians include the seven prominent features listed above, and Ar Heα that is required to fit the data between fluorescent Ar Kα and Ar Kβ. We adopted a broken power-law model for the continuum emission. In this way, we measured EWs for individual features. The results are summarized in Table 3.

3.2. Converting EWs to Abundances

The EWs were then converted to absolute elemental abundances. To this end, we calculated model EWs as a function of abundance to compare with our measurements. We adopted (1) a two-temperature (2T) model with two values of T and emission measure (EM), and (2) a multitemperature model with power-law dependence of the differential emission measure (DEM) on the temperature, i.e., EM = constant × T^{α}. Specifically, we used the `vapec` and `cevmkl` models in XSPEC for the 2T and DEM cases, respectively, where both models give an emission spectrum from collisionally ionized diffuse gas, using the atomic database version of ATOMDB3.0.3. Ideally, it would be best if we can constrain the two temperatures or the maximum temperature by our data themselves. This may be possible if we can perform detailed spectral fitting, taking account of the spectral deformation

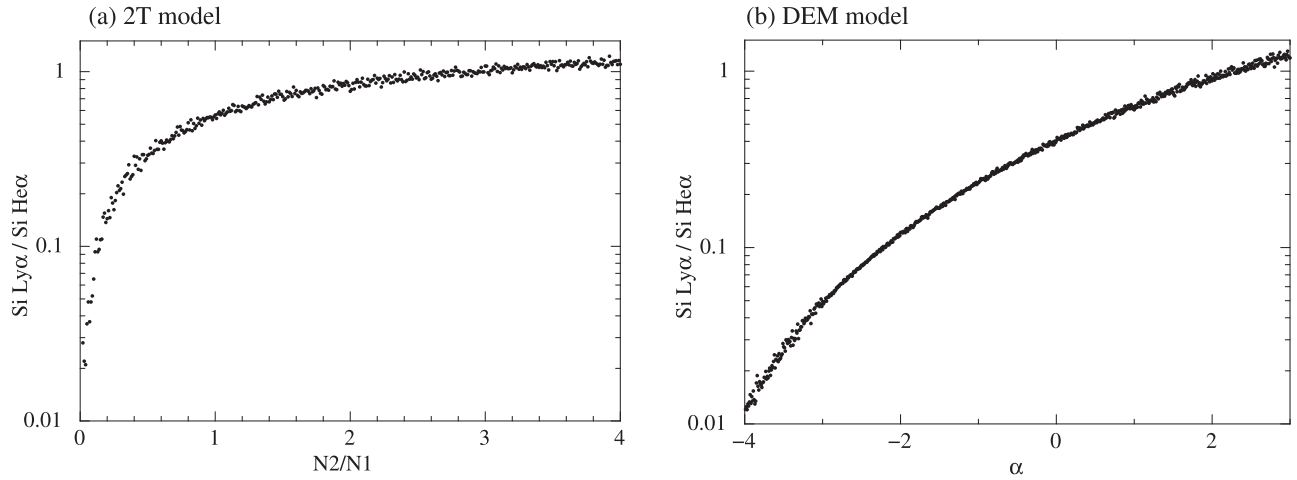

Figure 5. (a) Si Lyα/Si Heα ratio for the 2T model. The x-axis, N2/N1, is a normalization ratio between two `apec` components with temperatures of 1.7 and 0.5 keV (see the text for more details). The scatter of the data points is due to the statistical fluctuation arising from spectral fits to faked (simulated) XIS spectra. (b) Same as (a) but for the DEM model. The x-axis, α, is the index of the power-law temperature dependence of the EM.

Table 4
Si Lyα/Si Heα Ratios, N2/N1 for the 2T Model, and α for the DEM Model

Flare ID	Si Lyα/Si Heα	Albedo-corrected Si Lyα/Si Heα	N2/N1	α
Flare-1a	0.63 ± 0.05	0.50 ± 0.04	$0.84^{+0.10}_{-0.09}$	0.44 ± 0.17
Flare-1b	0.29 ± 0.02	0.23 ± 0.02	$0.32^{+0.02}_{-0.04}$	$-1.03^{+0.11}_{-0.12}$
Flare-1c	0.19 ± 0.03	0.15 ± 0.02	$0.20^{+0.03}_{-0.04}$	$-1.69^{+0.22}_{-0.23}$
Flare-2a	0.58 ± 0.03	0.46 ± 0.03	$0.75^{+0.06}_{-0.05}$	0.27 ± 0.12
Flare-2b	0.30 ± 0.02	0.24 ± 0.02	$0.33^{+0.03}_{-0.02}$	-0.96 ± 0.12
Flare-3a	0.73 ± 0.09	0.59 ± 0.08	$1.06^{+0.23}_{-0.19}$	$0.80^{+0.30}_{-0.31}$
Flare-3b	0.30 ± 0.02	0.24 ± 0.02	0.34 ± 0.03	-0.95 ± 0.12
Flare-3c	0.38 ± 0.04	0.31 ± 0.03	0.45 ± 0.06	$-0.53^{+0.18}_{-0.19}$
Flare-4a	1.01 ± 0.11	0.80 ± 0.09	$1.82^{+0.43}_{-0.36}$	$1.62^{+0.31}_{-0.33}$
Flare-4b	0.22 ± 0.03	0.18 ± 0.03	0.24 ± 0.04	$-1.44^{+0.22}_{-0.24}$

due to Earth albedo effects. However, such a sophisticated spectral modeling is beyond the scope of this paper. We thus assumed the temperatures (kT) of the 2T model to be 0.5 and 1.7 keV, based on previous studies showing a bimodal DEM with peak temperatures of those values (e.g., Caspi et al. 2014; Sylwester et al. 2014). As for the DEM model, we assumed $kT_{\rm max}$ to be 2 keV, because the lines of our interest (lines from He- and H-like ions of Si, S, Ar, and Ca) are formed by thermal plasmas with a temperature range of 0.2–2 keV. For X-class flares, there may be additional superhot ($kT \gtrsim 3$ keV) components (e.g., Caspi & Lin 2010). This component may contribute to the data to some extent, but not much in the energy range below 5 keV.

In our case of the 2T (0.5 keV + 1.7 keV) model or the DEM model, the EW depends not only on the elemental abundance but also on either the normalization ratio between the two components (N2/N1) or the index (α) of the power-law temperature distribution. Therefore, to convert EWs to absolute abundances, we need to know these parameters, which are sensitive to, and thus can be measured by, intensity ratios between lines from different charge states of the same element. To this end, we chose a Si Lyα/Si Heα intensity ratio, as it is best constrained in our data. Figure 5 illustrates how the Si Lyα/Si Heα depends on N2/N1 and α. Based on these plots combined with Si Lyα/Si Heα ratios, we assessed N2/N1 and α values for all the spectra, as in Table 4.

It should be noted that the Si Lyα/Si Heα ratio increases due to the Earth albedo (the effect of spectral hardening). To take this effect into account, we performed a Monte Carlo simulation. Details on the simulation are described in Appendix B. Briefly, the input of the simulation is the intrinsic solar X-ray spectrum, i.e., the `apec` model with a typical solar flare temperature of $kT = 1.5$ keV, and the output is an Earth albedo spectrum. The simulation indicated that the intrinsic Si Lyα/Si Heα are 0.8 times the albedo data, namely observations. We used the corrected Si Lyα/Si Heα ratios to infer the values of N2/N1 and α in Table 4.

We computed model EWs as a function of absolute abundances at the best-estimated N2/N1 (2T model) or α (DEM model) for individual spectra from Flare-1a to Flare-4b. In principle, the model EWs can be derived directly from the emission models, i.e., `vapec` and `cevmkl`. However, we "measured" the model EWs by fitting simulated XIS spectra with the same model as we used to measure EWs. This process is important especially for X-ray CCDs with moderate spectral resolution that cannot resolve individual lines; the Gaussians in our fitting include not only the main line(s) but also some other fainter lines that might affect the EW measurements. Therefore, we first generated model spectra convolved with the XIS response function by using the `fakeit` command in XSPEC. We then fitted the simulated XIS spectra with the same combination model as we did in our EW measurements for real data, obtaining model EWs. Figure 6 exhibits DEM-model-based EWs as a function of absolute abundance for Flares-1a, 1b, and 1c. Using these plots, we converted the EWs to absolute elemental abundances, which are summarized in Table 5. The uncertainties on the abundances estimated by varying the EWs within their uncertainties. Throughout this paper, we give the abundances relative to the photospheric values by Lodders (2003); $\rm Si/H = 3.47 \times 10^{-5}$, $\rm S/H = 1.55 \times 10^{-5}$, $\rm Ar/H = 3.55 \times 10^{-6}$, and $\rm Ca/H = 2.19 \times 10^{-6}$ in number. These values are in between the classical abundances by Anders & Grevesse (1989) and a more recent abundances by Asplund et al. (2009); the former gives $\rm Si/H = 3.55 \times 10^{-5}$, $\rm S/H = 1.62 \times 10^{-5}$, $\rm Ar/H = 3.63 \times 10^{-6}$, and $\rm Ca/H = 2.29 \times 10^{-6}$, whereas the latter gives $\rm Si/H = 3.24 \times 10^{-5}$, $\rm S/H = 1.32 \times 10^{-5}$, $\rm Ar/H = 2.51 \times 10^{-6}$, and $\rm Ca/H = 2.19 \times 10^{-6}$. Figure 7 shows the same absolute abundances as a function of time after flaring, where

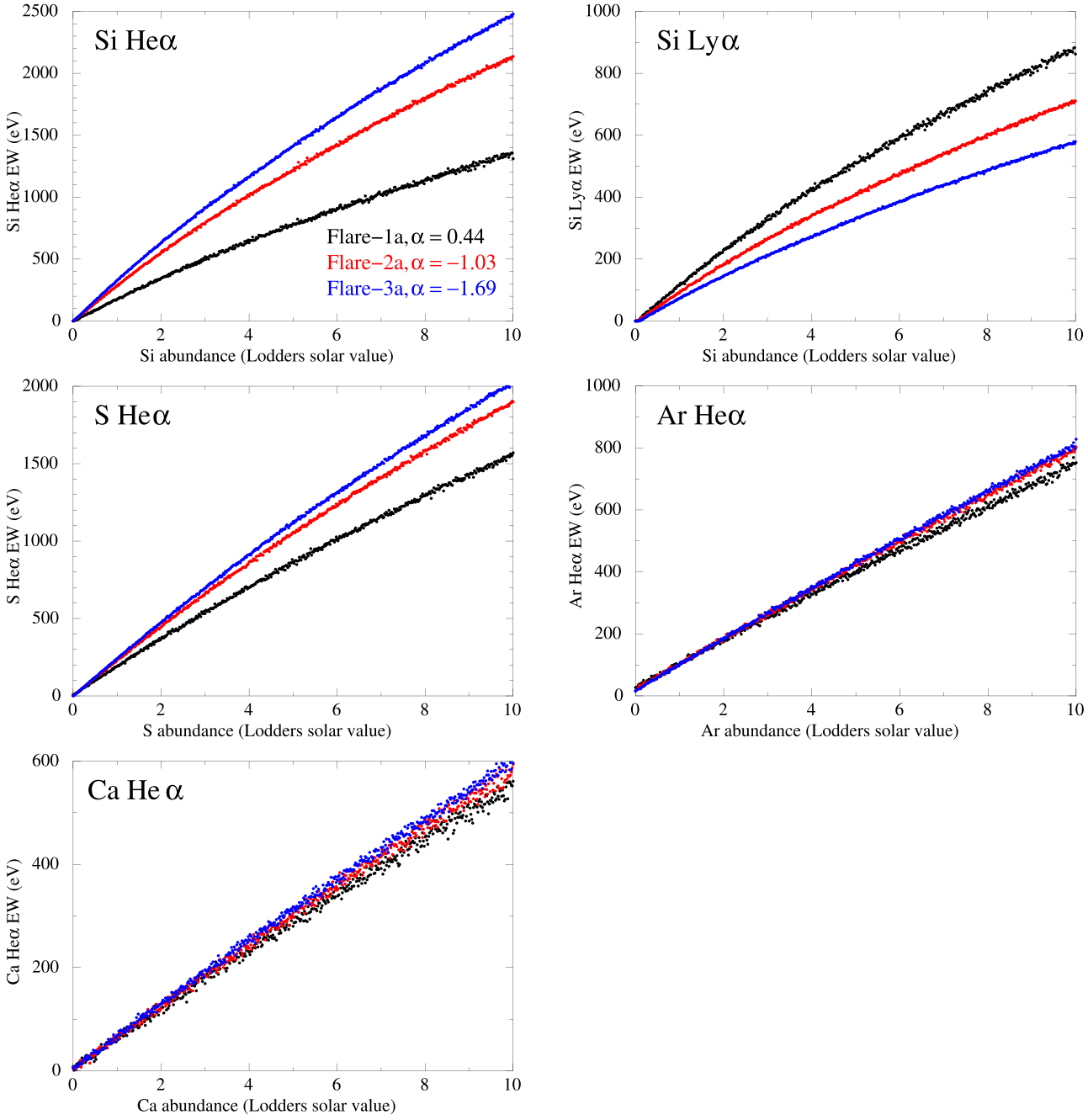

Figure 6. Equivalent widths as a function of metal abundances for Si Heα, Si Lyα, S Heα, Ar Heα, and Ca Heα. These are based on the DEM model, and the temperature slope parameters (α) are set to those for Flare-1 spectra. Black, red, and blue are responsible for Flare-1a, 1b, and 1c, respectively. Similarly to Figure 5, the scatter of the data points is the statistical fluctuation arising from spectral fits to faked spectra.

flaring times were defined as *GOES* X-ray rise-up times determined by eyes.

We confirmed that the Si Heα- and Si Lyα-based Si abundances generally agree with each other. This shows the robustness of our conversion process from EWs to abundances. Also, the two abundances derived from the 2T and DEM models are close to each other, showing the stability of the emission model assumed.

4. Discussion

In Figure 8, we plot the absolute abundances as a function of FIP measured at around each flare peak (i.e., Flare-1–Flare-4a spectra). The averaged elemental abundances are calculated to be Ca $\sim$ 2.0, Si $\sim$ 0.7, S $\sim$ 0.3, and Ar $\sim$ 0.9 solar photospheric values. This abundance pattern reminds us of the i-FIP effect with a turnover at the low end of FIP as observed in the coronae of several active stars (Osten et al. 2003; Sanz-Forcada et al. 2003; Argiroffi et al. 2004; Huenemoerder et al. 2013). In fact, such i-FIP effects from solar flares are consistent with the picture that high-/low-FIP enriched coronae feature a relative enrichment of low/high-FIP elements during flares (Nordon & Behar 2008). We note that their suggestion is mainly based on *Chandra* and *XMM-Newton* observations of stars, while they did include the Sun as one of the examples of low-FIP enriched coronae and high-FIP enhanced (relative to low-FIP elements) flares.

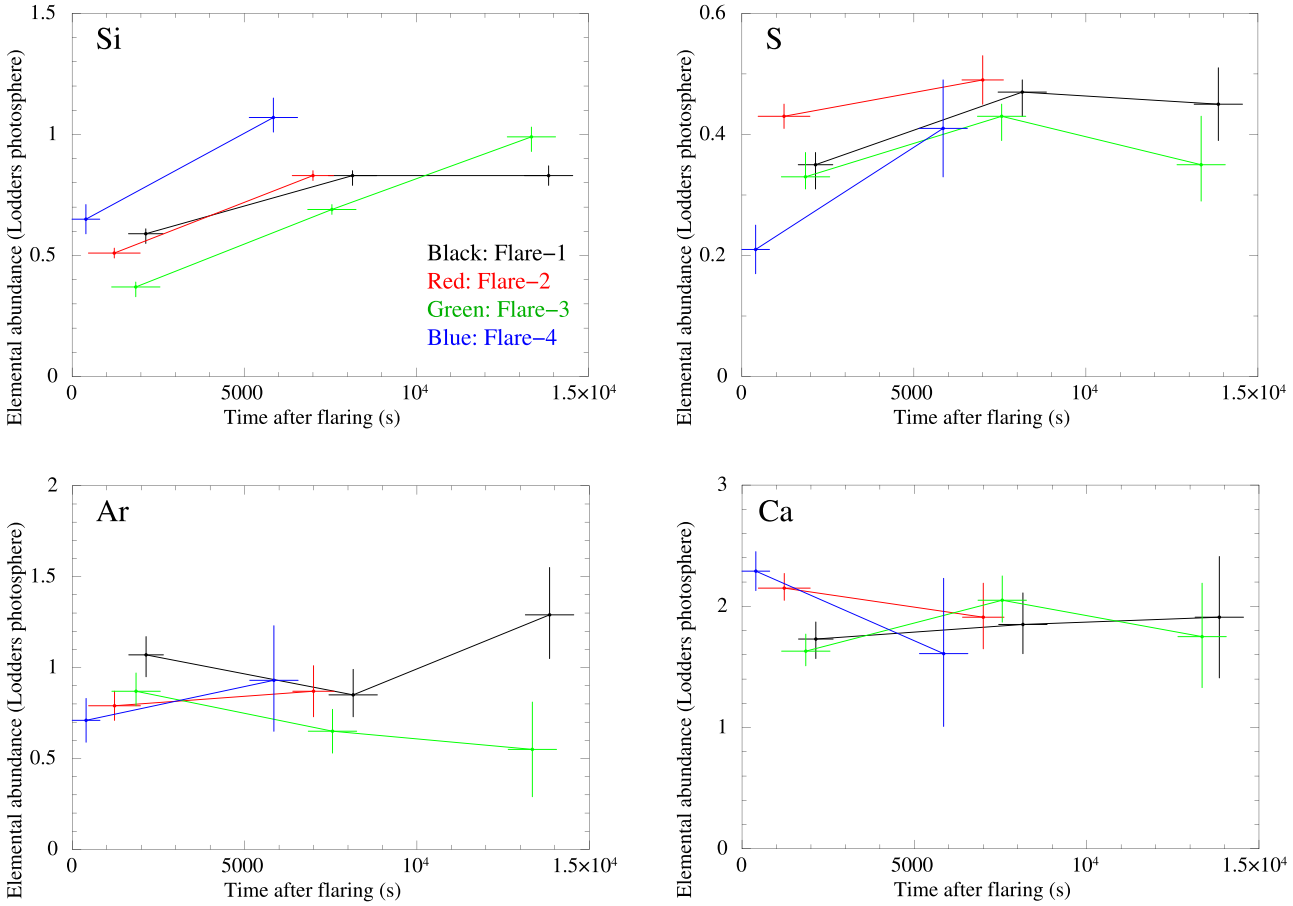

Figure 7. Elemental abundance (X/H) relative to the photospheric value as a function of time. Black, red, green, and blue correspond to Flares-1, 2, 3, and 4, respectively. These abundances are derived from the DEM model. The Si abundance is based on the Si Heα.

In the decay phase of the flares, the Si abundance significantly increases up to ∼2 times the initial value, so that the abundance approaches the coronal abundance. The same trend can be seen for S as well. This abundance evolution is also seen for flares in other stars; the abundance pattern exhibits the strong i-FIP/FIP effect during flare peaks, and then evolves toward the preflare FIP/i-FIP basal state (e.g., Tsuru et al. 1989; Stern et al. 1992; Pan et al. 1997; Tsuboi et al. 1998; Favata et al. 2000; Liefke et al. 2010). These properties can be explained by the scenario that the excess emission of flares is caused by the chromospheric evaporation, as discussed in Nordon & Behar (2008).

A similar Fe (a low-FIP element with FIP = 7.9 eV) abundance increase during solar flares was found by Warren (2014) who measured absolute abundances for 21 M9.3 to X6.9 class flares using *Solar Dynamics Observatory*/EUV Variability Experiment spectra. On the other hand, such low-FIP increases were not seen in many other observations of solar flares (e.g., Narendranath et al. 2014; Dennis et al. 2015; Sylwester et al. 2015). The reason of such flare-to-flare variations is unclear, but one notable difference is the flare size; those investigated by this work and Warren (2014) are generally larger than those by others. We speculate that the composition of larger flares tends to show a greater departure (or a clearer i-FIP effects) compared with those in coronae. As a result, they may show significant abundance evolution toward preflare states in the decay phase.

It is interesting to compare our results with i-FIP patches recently discovered near sunspots during solar flares (e.g., Doschek et al. 2015). First, the composition is different between the i-FIP patches and the flares of our interest. The i-FIP patches exhibit anomalously high Ar XIV/Ca XIV intensity ratios, with an extreme case that the measured relative Ar/Ca abundance is about 10 (30) times the photospheric (coronal) value. This does not agree with our measured Ar/Ca ratios of about three times the solar photospheric value. In addition, the absolute abundance of Ca (Ca/H) appears to differ as well. At the i-FIP patches, there are two independent arguments that the Ca abundance is depleted, which makes the relative Ar/Ca abundance very high, as observed (Doschek & Warren 2016; Brooks 2018). This would disagree with our measurement, i.e., Ca/H ∼ 2 times the photospheric value. These composition differences are not surprising, given that our data are spatially unresolved, full disk integration, whereas the i-FIP patches are highly localized small regions. The i-FIP patches would perhaps not make a significant contribution to the total X-ray emission from flares.

The composition difference between i-FIP patches and our measurements could be explained by different turnover FIPs, by analogy to various turnover FIPs observed in active stars: a turnover above Al (FIP = 6.0 eV), Ca (FIP = 6.1 eV), Na (FIP = 5.1 eV), and K (FIP = 4.3 eV) for σ^2 CrB (Osten et al. 2003), AB Dor (Sanz-Forcada et al. 2003), PZ Tel (Argiroffi et al. 2004), and σ Gem (Huenemoerder et al. 2013), respectively. Namely, the i-FIP patches would have a

Table 5
Elemental Abundances[a]

Flare ID (Emission Model)	Si Heα	Si Lyα	S Heα	Ar Heα	Ca Heα
Flare-1a (2T)	$0.77^{+0.03}_{-0.04}$	0.81 ± 0.04	$0.47^{+0.03}_{-0.04}$	1.06 ± 0.11	$1.48^{+0.12}_{-0.14}$
Flare-1a (DEM)	$0.59^{+0.02}_{-0.04}$	0.63 ± 0.04	$0.35^{+0.02}_{-0.04}$	$1.07^{+0.10}_{-0.12}$	$1.73^{+0.14}_{-0.16}$
Flare-1b (2T)	1.06 ± 0.04	1.15 ± 0.07	0.68 ± 0.05	0.92 ± 0.14	$1.69^{+0.25}_{-0.24}$
Flare-1b (DEM)	$0.83^{+0.02}_{-0.04}$	$0.87^{+0.06}_{-0.04}$	$0.47^{+0.02}_{-0.04}$	$0.85^{+0.14}_{-0.12}$	$1.85^{+0.26}_{-0.24}$
Flare-1c (2T)	0.99 ± 0.05	1.06 ± 0.15	0.62 ± 0.08	1.48 ± 0.29	$1.83^{+0.52}_{-0.51}$
Flare-1c (DEM)	0.83 ± 0.04	$0.87^{+0.12}_{-0.14}$	0.45 ± 0.06	$1.29^{+0.26}_{-0.24}$	1.91 ± 0.50
Flare-2a (2T)	$0.68^{+0.02}_{-0.03}$	$0.71^{+0.03}_{-0.02}$	0.57 ± 0.03	$0.77^{+0.08}_{-0.07}$	$1.88^{+0.09}_{-0.10}$
Flare-2a (DEM)	0.51 ± 0.02	0.55 ± 0.02	0.43 ± 0.02	0.79 ± 0.08	$2.15^{+0.12}_{-0.10}$
Flare-2b (2T)	1.06 ± 0.03	$1.17^{+0.07}_{-0.08}$	$0.69^{+0.05}_{-0.04}$	0.95 ± 0.15	$1.69^{+0.27}_{-0.25}$
Flare-2b (DEM)	0.83 ± 0.02	$0.89^{+0.04}_{-0.06}$	0.49 ± 0.04	0.87 ± 0.14	$1.91^{+0.28}_{-0.26}$
Flare-3a (2T)	0.48 ± 0.04	$0.49^{+0.04}_{-0.03}$	0.45 ± 0.04	$0.82^{+0.10}_{-0.09}$	$1.33^{+0.13}_{-0.11}$
Flare-3a (DEM)	$0.37^{+0.02}_{-0.04}$	0.39 ± 0.04	$0.33^{+0.04}_{-0.02}$	$0.87^{+0.10}_{-0.08}$	$1.63^{+0.14}_{-0.12}$
Flare-3b (2T)	$0.89^{+0.02}_{-0.03}$	0.97 ± 0.06	$0.61^{+0.03}_{-0.05}$	$0.70^{+0.14}_{-0.13}$	$1.84^{+0.20}_{-0.18}$
Flare-3b (DEM)	0.69 ± 0.02	$0.73^{+0.06}_{-0.04}$	$0.43^{+0.02}_{-0.04}$	0.65 ± 0.12	$2.05^{+0.20}_{-0.18}$
Flare-3c (2T)	$1.27^{+0.07}_{-0.06}$	1.42 ± 0.12	0.52 ± 0.10	$0.56^{+0.29}_{-0.31}$	1.54 ± 0.40
Flare-3c (DEM)	$0.99^{+0.04}_{-0.06}$	$1.07^{+0.10}_{-0.08}$	$0.35^{+0.08}_{-0.06}$	0.55 ± 0.26	$1.75^{+0.44}_{-0.42}$
Flare-4a (2T)	0.82 ± 0.07	$0.81^{+0.05}_{-0.04}$	0.27 ± 0.04	$0.61^{+0.11}_{-0.12}$	1.91 ± 0.14
Flare-4a (DEM)	0.65 ± 0.06	$0.69^{+0.06}_{-0.04}$	0.21 ± 0.04	0.71 ± 0.12	2.29 ± 0.16
Flare-4b (2T)	$1.31^{+0.09}_{-0.08}$	$1.40^{+0.20}_{-0.18}$	$0.58^{+0.10}_{-0.11}$	$1.04^{+0.36}_{-0.33}$	$1.50^{+0.61}_{-0.60}$
Flare-4b (DEM)	$1.07^{+0.08}_{-0.06}$	$1.11^{+0.16}_{-0.14}$	0.41 ± 0.08	$0.93^{+0.30}_{-0.28}$	$1.61^{+0.62}_{-0.60}$

Note.
[a] Relative to the solar photospheric values by Lodders (2003).

particularly low turnover FIP below Ca, whereas most of the flaring region (responsible for our observations) would have a relatively high turnover FIP between Ca and Si (FIP $= 8.2$ eV). Understanding the origin of such a turnover and its spatial variation is left as important future work.

One important question about the i-FIP patches in past observations was which element is enhanced and which element is depleted. Based on direct measurements of EWs, combined with emission models of either a two-temperature model or a multitemperature model with power-law dependence of the differential emission measure on the temperature, we revealed that the Si abundance is depleted around flare peaks when the i-FIP effect becomes evident. This is consistent with the ponderomotive fractionation model proposed by Laming (2004, 2012, 2015, 2017), in which the ponderomotive force, which can be directed either upward or downward depending on the situation, can act only on low-FIP elements, so that enhanced and depleted low-FIP elements are expected for FIP and i-FIP effects, respectively, with high-FIP elements unmodified. The transition from depletion to enhancement of the Si abundance in the decay phases of the flares would be caused by plasma mixing with the surrounding FIP biased plasmas, as was proposed to explain fading i-FIP patches (Baker et al. 2019).

We point out that the absolute abundances vary from flare to flare by a factor of two with no correlations with other physical parameters such as the flare class and temperature. This is consistent with previous results (e.g., Sylwester et al. 1998). On the other hand, we argued that i-FIP effects may be present only for giant flares in their early phases. Therefore, there might be an anticorrelation between the absolute abundance and the flare class, if we accumulate a large range of flare classes and focus on the initial phase of flares.

Finally, we note that the *X-Ray Imaging Spectroscopy Mission* (*XRISM*: Tashiro et al. 2018), the Japan–US X-ray astronomy mission scheduled to be launched in early 2022, will

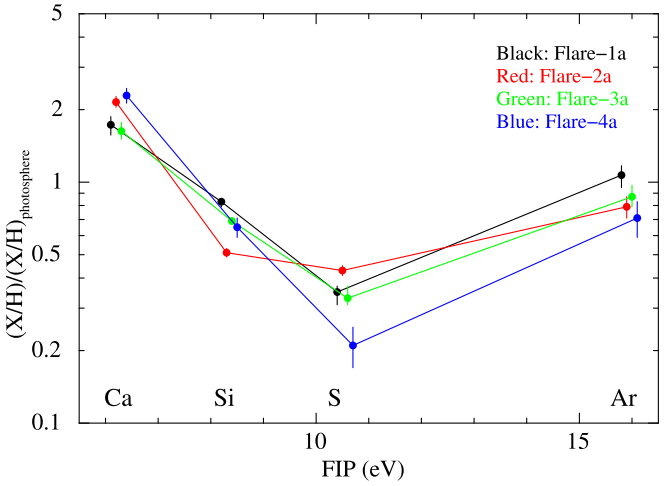

Figure 8. Absolute elemental abundances as a function of FIP. Black, red, green, and blue correspond to Flares-1, 2, 3, and 4, respectively. For clarity, we introduce an offset in FIP by +0.1 eV. These abundances are derived from the DEM model. The Si abundance is based on the Si Heα.

dramatically improve abundance studies for solar flares and corona. *XRISM* will be in the same low-Earth orbit as *Suzaku*, allowing for a long-term, 96 minutes cadence monitoring of the Sun via Earth albedo as a by-product. Thanks to the superior energy resolution, FWHM $\lesssim 7$ eV (or $E/\Delta E \sim 600$ at 3 keV) with little energy dependence in 0.2–12 keV, of the X-ray microcalorimeter on board *XRISM*, we will be able to detect many more lines than *Suzaku*/XIS. These include lines from many elements such as C, N, O, Ne, Na, Mg, Al, Fe, and Ni in addition to the four abundant intermediate-mass elements analyzed in this paper. Therefore, we will be able to obtain detailed abundance patterns from individual flares, as with the cases of the high-resolution X-ray spectroscopy of stellar

coronae with gratings on board *Chandra* and *XMM-Newton*. Furthermore, fluorescent lines of N, O, and Ar from the Earth's atmosphere will be clearly detected. These will provide us with intriguing information about upper atmosphere of the Earth.

5. Conclusion

We performed X-ray spectroscopy of four X-class flares, using Earth albedo data obtained with *Suzaku*/XIS. The good energy resolution and low background of *Suzaku*/XIS allow several features and underlying continuum emission to be clearly detected. We measured EWs of line features from intermediate-mass elements, i.e., Si, S, Ar, and Ca, and converted them to the absolute abundances (X/H). The absolute elemental abundances averaged over the four flares are obtained to be ∼2.0 (Ca), ∼0.7 (Si), ∼0.3 (S), and ∼0.9 (Ar) at around flare peaks. This abundance pattern is consistent with i-FIP effects seen in active stars' coronae. The depletion of Si (and S) is consistent with the Laming model to explain both FIP and i-FIP effects observed in stellar coronae. The abundances are almost constant during the flares, whereas Si increases by a factor of ∼2 in the decay phase. Such Si abundance evolution is consistent with a picture that the i-FIP plasma originates from chromospheric evaporation and then mixes with the surrounding low-FIP biased materials.

We thank Dr Hideki Uchiyama and Dr Makoto Sawada for discussions about self-charge-filling effects of the XIS and the equivalent widths using XSPEC and SPEX codes, respectively. This work was supported by the Japan Society for the Promotion of Science KAKENHI grant Nos. JP17H02864 (S.K.), 16H03983 (K.M.), 17K05392 (Y.T.), 17K05393 (K.S.), 18K18767, 19H01908, 19H00696 (K.H.), and 18H01256 (H. N.). This work was partly supported by the Leading Initiative for Excellent Young Researchers, MEXT, Japan. The research of M.O. has been supported by the European Union, co-financed by the European Social Fund (research and development activities at the Eötvös Loránd University's Campus in Szombathely, EFOP-3.6.1-16-2016-00023).

Appendix A
A New Method to Estimate the Dark Level of the XIS

The telemetry of each event in the *Suzaku* XIS data analyzed here contains the dark-subtracted PH values of nine pixels, which are the event center pixel and the neighboring eight pixels. The energy value of each event is reconstructed from the nine PH values in the ground processing based on the grade method.[19] The event telemetry also contains two kinds of information about the surrounding 16 pixels, *pOuterMost* and *sumOuterMost*. *pOuterMost* is a 16 bit "hit pattern" identifying which surrounding pixels have a PH value grater than the threshold. *pOuterMost* is also used for event grading. *sumOuterMost* is the summed PH value of all the surrounding pixels that have a PH value less than or equal to the threshold. Note that the value of *sumOuterMost* would be around zero within statistical fluctuation if the onboard dark estimation follows the actual CCD pedestal value reasonably well. If not, *sumOuterMost* would have a significant offset from zero either positively or negatively. This situation could happen in the case that the background level varies more rapidly than the onboard dark estimation could follow. Since the number of surrounding pixels contributing *sumOuterMost* can be known from *pOuterMost*, we can measure the amount of the deviation of the onboard dark estimation from the actual CCD pedestal value per pixel, correct the PH values of the nine central pixels by the amount, and recalculate the energy value of the event based on the corrected PH values.

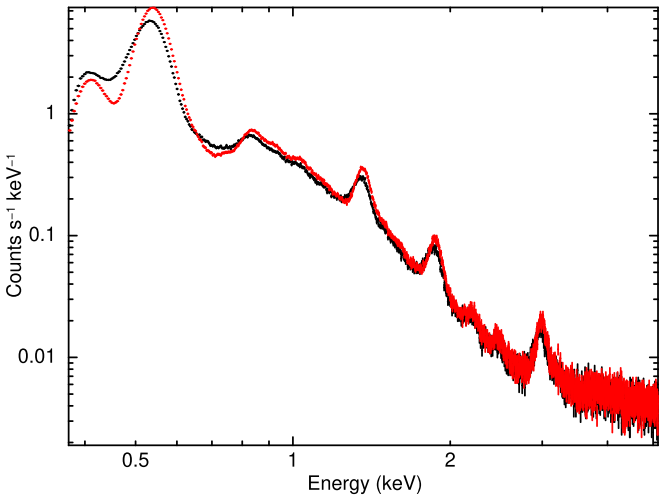

Figure 9. Comparison of the bright Earth data spectra before (black) and after (red) correction. This is the XIS0 case.

Figure 9 shows a comparison of the bright Earth data spectra before and after applying the correction described here. All the line structures become sharper after the correction, indicating the validity of this method. The sharpness is more evident in the lower energy lines since the ratio of the amount of the correction to the event PH is relatively larger in the lower energy events. We confirm that this method is efficient only for the bright Earth data; no improvement can be seen for the standard data in which the satellite is pointing at the astronomical objects or the dark side of the Earth. This fact indicates that the onboard dark estimation of the *Suzaku* XIS works well for the standard data and that the intense optical light flux, which is the major source to change the CCD pedestal value in the bright Earth data, varies more rapidly than the onboard dark estimation.

Appendix B
Monte Carlo Simulation to Take Account of Earth Albedo Effects

The spectral hardening due to the reflection by the Earth's albedo would expect to increase the Si Lyα/Si Heα line ratio and this effect should be taken into account when interpreting the data. Since the calculation procedures of the reflected X-ray spectrum by the Earth's albedo is complicated due to various scattering processes such as Thomson scattering and Compton scattering, a Monte Carlo simulation including the intrinsic solar X-ray spectrum and a relevant air composition of the Earth is an appropriate approach to estimate an expected scattered X-ray spectrum. In this paper, we performed a Monte Carlo simulation based on the GEANT4 toolkit library (version 10.04) (Apostolakis et al. 2003; Allison et al. 2006, 2013), which is commonly used to perform full Monte Carlo simulations including complicated geometries. In this simulation framework, we input photons with the energy spectrum from collisionally ionized diffuse gas, named as `apec`, which

[19] See the *Suzaku* technical description for details, https://heasarc.gsfc.nasa.gov/docs/suzaku/prop_tools/suzaku_td/.

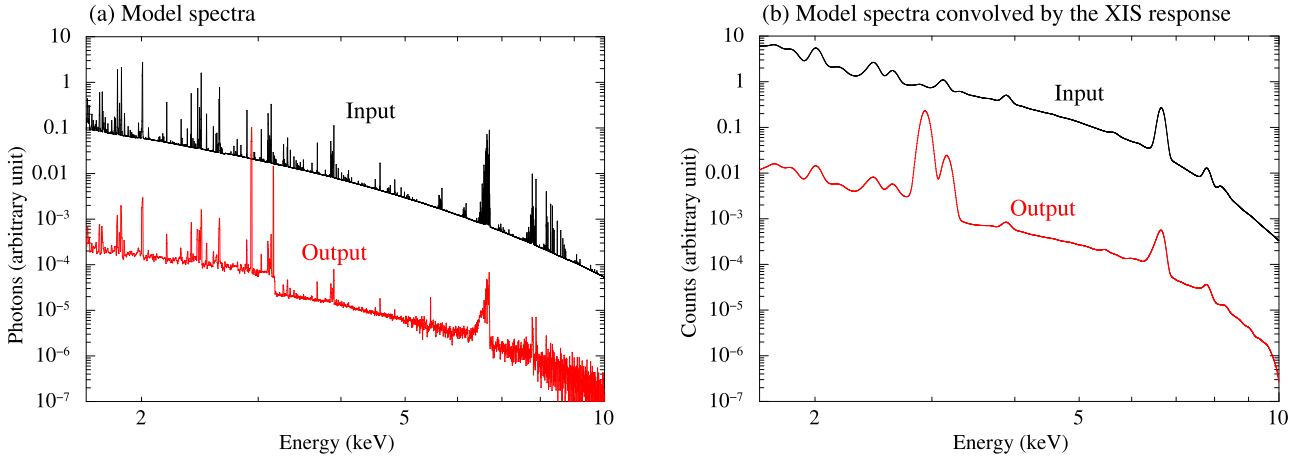

Figure 10. (a) Comparison of the photon spectrum emitted from ionized diffuse gas with a temperature of 1.5 keV calculated by the `apec` model without scattering effect (black) to the simulated photon spectrum after scattering by the Earth's atmosphere (red). (b) Same as (a), but the data are convolved by the detector response of *Suzaku* XIS.

is calculated by the atomic database with the XSPEC software package (Arnaud 1996). The atomic database version for the simulation is ATOMDB2.0.2, which is different from that used for the X-ray data analysis in Section 3.1. We confirmed that the model spectrum in 1–5 keV shows no significant differences between ATOMDB2.0.2 and 3.0.3, and thus we conclude that our simulation using ATOMDB2.0.2 can be applied for comparison to the data analysis.

We assume a typical solar flare temperature of $kT = 1.5$ keV (see Section 3.1) with an abundance of solar photospheric values. Photons are generated enough far from the Earth like a point source. The generated photon interacts the Earth atmosphere in the simulation. The Earth's atmosphere is composed of oxygen and nitrogen atoms and molecules, as well as argon atoms, which were all included in the simulation. The density profile of each component is taken into account by implementing the 10 km thickness of sphere-shell-shape geometry up to 300 km altitude. It is known that the density profile would change slightly depending on the solar activity. We confirmed that our simulation result is not affected by this effect. Therefore, we apply the density profile obtained during a solar maximum period, 2013 August 1, which is provided by the publicly available NRLMSISE-00 atmosphere model.[20]

Since what we have to know is the X-ray spectrum reflected by the Earth's albedo, we accumulated photons only scattered by the Earth's atmosphere. For this purpose, we put the photon detector at 500 km altitude in the simulation and recorded the photons only with an angle between the incident and detected position larger than $\pi/2$. Figure 10(a) shows the example of the input and the scattered X-ray spectrum, in which we can see that the hardening of the continuum as well as some changes of line ratios due to the scattering. The simulated X-ray reflection spectrum is converted to the XSPEC table model, so that we can estimate the line ratio by convolving with the detector response of the *Suzaku* XIS as shown in Figure 10(b). It should be noted that the solar X-ray scattering angles are around 110° in our cases (see Table 1). We confirmed, however, that there is no obvious spectral difference around 2 keV between reflection angles of 90°–180° and 105°–115°.

[20] https://ccmc.gsfc.nasa.gov/modelweb/models/nrlmsise00.php (Labitzke et al. 1985; Hedin 1991; Picone et al. 2002).

ORCID iDs

Satoru Katsuda https://orcid.org/0000-0002-1104-7205
Makoto S. Tashiro https://orcid.org/0000-0002-5097-1257
Yukikatsu Terada https://orcid.org/0000-0002-2359-1857
Yohko Tsuboi https://orcid.org/0000-0001-9943-0024
Takaaki Yokoyama https://orcid.org/0000-0001-5457-4999

References

Allison, J., Amako, K., Apostolakis, J., et al. 2006, ITNS, 53, 270
Allison, J., Amako, K., Apostolakis, J., et al. 2013, NIMA, 835, 186
Anders, E., & Grevesse, N. 1989, GeCoA, 53, 197
Apostolakis, J., Allison, J., Amako, K., et al. 2003, NIMA, 506, 250
Argiroffi, C., Drake, J. J., Maggio, A., et al. 2004, ApJ, 609, 925
Arnaud, K. A. 1996, ASPC, 101, 17
Asplund, M., Grevesse, N., Sauval, A. J., & Scott, P. 2009, ARA&A, 47, 481
Audard, M., Güdel, M., Sres, A., Raassen, A. J. J., & Mewe, R. 2003, A&A, 398, 1137
Baker, D., van Driel-Gesztelyi, L., Brooks, D. H., et al. 2019, ApJ, 875, 35
Brinkman, A. C., Behar, E., Güdel, M., et al. 2001, A&A, 365, L324
Brooks, D. H. 2018, ApJ, 863, 140
Caspi, A., & Lin, R. P. 2010, ApJL, 725, L161
Caspi, A., McTiernan, J. M., & Warren, H. P. 2014, ApJL, 788, L31
Caspi, A., Woods, T. N., & Warren, H. P. 2015, ApJL, 802, L2
Dennis, B. R., Phillips, K. J. H., Schwartz, R. A., et al. 2015, ApJ, 803, 67
Doschek, G. A., & Warren, H. P. 2016, ApJ, 825, 36
Doschek, G. A., Warren, H. P., & Feldman, U. 2015, ApJL, 808, L7
Drake, J. J., Laming, J. M., & Widing, K. G. 1997, ApJ, 478, 403
Favata, F., Reale, F., Micela, G., et al. 2000, A&A, 353, 987
Feldman, U. 1992, PhyS, 46, 202
Feldman, U., & Widing, K. G. 1993, ApJ, 414, 381
Fludra, A., & Schmelz, J. T. 1999, A&A, 348, 286
Güdel, M., Audard, M., Briggs, K., et al. 2001, A&A, 365, L336
Hedin, A. E. 1991, JGR, 96, 1159
Henoux, J.-C. 1998, SSRv, 85, 215
Huenemoerder, D. P., Canizares, C. R., Drake, J. J., & Sanz-Forcada, J. 2003, ApJ, 595, 1131
Huenemoerder, D. P., Phillips, K. J. H., Sylwester, J., & Sylwester, B. 2013, ApJ, 768, 135
Ishisaki, Y., Maeka, Y., Fujimoto, R., et al. 2007, PASJ, 59, S113
Itoh, M., Yamada, H., Ishisaki, Y., et al. 2002, in IAU 8th Asian-Pacific Reg. Meeting, II, ed. S. Ikeuchi, J. Hearnshaw, & T. Hanawa (Tokyo: Astronomical Society of Japan), 435
Koyama, K., Tsunemi, H., Dotani, T., et al. 2007, PASJ, 59, S23
Labitzke, K., Barnett, J. J., & Edwards, B. 1985, Handbook MAP 16, SCOSTEP (Urbana, IL: Univ. Illinois), 16
Laming, J. M. 2004, ApJ, 614, 1063
Laming, J. M. 2009, ApJ, 695, 954
Laming, J. M. 2012, ApJ, 744, 115
Laming, J. M. 2015, LRSP, 12, 2

Laming, J. M. 2017, ApJ, 844, 153
Laming, J. M., & Drake, J. J. 1999, ApJ, 516, 324
Liefke, C., Fuhrmeister, B., & Schmitt, J. H. M. M. 2010, A&A, 514, A94
Lodders, K. 2003, ApJ, 591, 1220
Maeda, Y., Uchiyama, Y., Bamba, A., et al. 2009, PASJ, 61, 1217
Meyer, J.-P. 1985, ApJS, 57, 173
Mitsuda, K., Bautz, M., Inoue, H., et al. 2007, PASJ, 59, S1
Narendranath, S., Sreekumar, P., Alha, L., et al. 2014, SoPh, 289, 1585
Nordon, R., & Behar, E. 2008, A&A, 482, 639
Osten, R. A., Ayres, T. R., Brown, A., et al. 2003, ApJ, 582, 1073
Pan, H. C., Jordan, C., Makishima, K., et al. 1997, MNRAS, 285, 735
Phillips, K. J. H., & Dennis, B. R. 2012, ApJ, 748, 52
Picone, J. M., Hedin, A. E., Drob, D. P., & Aikin, A. C. 2002, JGR, 107, 1468
Raymond, J. C., Kohl, J. L., Noci, G., et al. 1997, SoPh, 175, 645
Reames, D. V. 2018, SSRv, 214, 61
Sanz-Forcada, J., Maggio, A., & Micela, G. 2003, A&A, 408, 1087
Schmelz, J. T., Reames, D. V., von Steiger, R., & Basu, S. 2012, ApJ, 755, 33
Sterling, A. C., Doschek, G. A., & Feldman, U. 1993, ApJ, 404, 394
Stern, R. A., Uchida, Y., Tsuneta, S., & Nagase, F. 1992, ApJ, 400, 321
Sylwester, B., Phillips, K. J., Sylwester, J., & Kepa, A. 2015, ApJ, 805, 49
Sylwester, B., Sylwester, J., Phillips, K. J. H., et al. 2014, ApJ, 787, 122
Sylwester, J., Kepa, A., & Bentley, R. D. 2002, AdSpR, 30, 105
Sylwester, J., Lemen, J. R., & Bentley, R. D. 1998, ApJ, 501, 397
Takahashi, T., Abe, K., Endo, M., et al. 2007, PASJ, 59, S35
Tashiro, M., Maejima, H., Toda, K., et al. 2018, Proc. SPIE, 10699, 1069922
Tawa, N., Hayashida, K., Nagai, M., et al. 2008, PASJ, 60, S11
Tsuboi, Y., Koyama, K., Murakami, H., et al. 1998, ApJ, 503, 894
Tsuru, T., Makishima, K., Ohashi, T., et al. 1989, PASJ, 41, 679
Veck, N. J., & Parkinson, J. H. 1981, MNRAS, 197, 41
Warren, H. P. 2014, ApJL, 786, L2
Wood, B. E., Laming, J. M., Warren, H. P., & Poppenhaeger, K. 2018, ApJ, 862, 66
Wood, B. E., & Linsky, J. L. 2010, ApJ, 717, 1279